



Optimal design of a cellular material encompassing negative stiffness elements for unique combinations of stiffness and elastic hysteresis

Anna Guell Izard ^a, Ricardo Fabian Alfonso ^a, Geoffrey McKnight ^b, Lorenzo Valdevit ^{a,*}

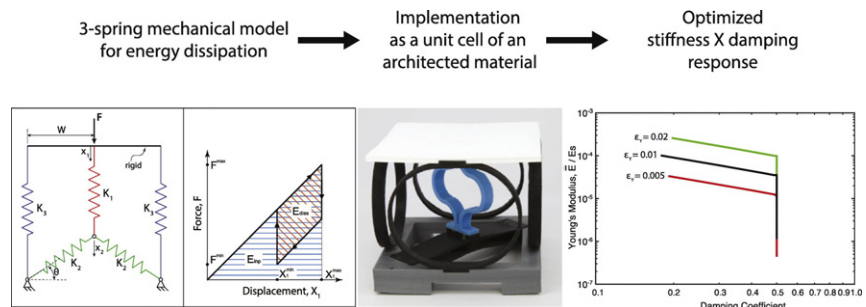
^a Mechanical and Aerospace Engineering Department, University of California, Irvine, United States

^b HRL Laboratories, Malibu, CA, United States

HIGHLIGHTS

- We present a 3-spring model with a negative stiffness element for energy dissipation.
- An architected material implementation of the model is designed and fabricated.
- The performance of the architected material is modeled and verified experimentally.
- The geometry of the architected material is optimized for stiffness and damping.
- This tunable stiff damper can be easily manufactured in virtually any material.

GRAPHICAL ABSTRACT



ARTICLE INFO

Article history:

Received 6 June 2017

Received in revised form 13 August 2017

Accepted 1 September 2017

Available online 5 September 2017

Keywords:

Negative stiffness

Energy dissipation

Optimization

Mechanical metamaterial

Finite element analysis

ABSTRACT

Viscoelastic materials are commonly used to dissipate kinetic energy in case of impact and vibrations. Unfortunately, dissipating large amounts of energy in a monolithic material requires high combinations of two intrinsic properties – Young's modulus and loss factor, which are generally in conflict. This limitation can be overcome by designing cellular materials incorporating negative stiffness elements. Here we investigate a configuration comprising two positive stiffness elements and one negative stiffness element. This unit cell possesses an internal degree of freedom, which introduces hysteresis under a loading-unloading cycle, resulting in substantial energy dissipation, while maintaining stiffness. We demonstrate and optimize a simple implementation in a single material design that does not require external stabilization or pre-compression of buckled elements; these key features make it amenable to fabrication by virtually any additive manufacturing approach (from 3D printing to assembly and brazing) in a wide range of base materials (from polymers to metals). No additional intrinsic damping mechanism is required for the base material, which is assumed linear elastic. Furthermore, the architected material can be designed to be fully recoverable. When optimized, these architected materials exhibit extremely high combinations of Young's modulus and damping, far superior to those of each constituent phase.

© 2017 Elsevier Ltd. All rights reserved.

1. Introduction

The ability to dissipate kinetic energy resulting from impact or vibration is a key requirement for a number of applications in aerospace and mechanical engineering. This energy can be dissipated

in a non-recoverable way, e.g., by plastic deformation [1,2], or in a recoverable manner, generally using viscoelastic materials [3]. Recoverable behavior is generally preferred, but the amount of energy that can be dissipated using viscoelastic materials is limited by the product of Young's modulus and loss factor [4].

In recent years, a number of novel architected materials have been introduced that are based on elastic constituent phases, yet achieve hysteretic behavior under cyclic loading (and hence energy dissipation).

* Corresponding author.

E-mail address: Valdevit@uci.edu (L. Valdevit).

Notable examples are hollow micro and nano-lattices with extremely low density which dissipate energy through internal vibration following the local buckling of the hollow bars, while maintaining linear elastic response at the constituent level up to extremely large effective strains [5,6]. Unfortunately this mechanism requires extremely low relative densities, and hence is not applicable to materials with significant strength and stiffness requirements. An alternative design is provided by entangled-wire or woven materials, which damp vibration through internal friction [7,8]. Contrary to hollow microlattices, these architected materials are generally very dense, resulting in heavier systems.

An energy dissipating mechanism that can overcome the challenges listed above is based on the snap-through buckling of elastic structural components with non-convex strain energy landscape [9,10], resulting in regimes of negative stiffness. Negative stiffness is a reversal of the usual directional relationship between force and displacement, which generally manifest itself in externally stabilized, displacement controlled structures over a range of displacements [11]: two pin-jointed springs with a non-zero initial angle, and an arch or a post-buckled beam undergoing snap-through (Fig. 1) are some examples of this concept.

The design of structures incorporating negative stiffness elements has been investigated over the past two decades, in particular with the goal of designing isolators [12–16]. Applications include seats [17, 18], earthquake protection [19] and ultra-sensitive optical devices [20]. The common configuration for a zero stiffness isolator consist of an arrangement of a positive and a negative stiffness element, combined in parallel. Tuning of the load-displacement curves for the springs can result in an effective load-displacement profile for the system featuring a flat plateau at the desired isolation force.

Recently, a number of investigators have studied simple arrangements of positive and negative stiffness elements to design structures and periodic architected materials with extreme damping. The simplest configuration consists of a stack of non-convex strain energy elements arranged in series. Notable implementations of this concept are reported in [10,9, 21,22] to design and realize cellular materials with high energy dissipation. In [23], superior damping performance was achieved by exploiting the unique post-buckling behavior of a free-end column. More complex mechanical models, consisting of series and parallel arrangements of positive and negative stiffness elements, have also been investigated [24–26]. These systems possess an internal degree of freedom that can be tuned to dramatically enhance the intrinsic loss factor of the base material under dynamic cyclic loadings. In [27], a clever implementation of a similar arrangement is used to realize an architected material that simultaneously exhibits negative stiffness and negative Poisson's ratio.

In this article, we propose and investigate a novel periodic cellular material configuration which allows independent control of stiffness and loss factor under cyclic loadings. In this novel design, each unit cell contains a particular arrangement of structural elements (henceforth called '3-spring configuration'), consisting in a positive stiffness element connected in series with a bi-stable (non-convex strain energy) element (possibly implemented by two pin-jointed springs at an angle), with the pair connected in parallel with a second positive stiffness element (Fig. 2a). This system of springs possesses an internal degree of freedom (point B), and consequently, when properly tuned, will exhibit hysteretic behavior under quasi-static cyclic loading, as schematically depicted in Fig. 2b. Clearly, the area under the hysteresis loop represents the energy dissipated in each cycle.

Although apparently similar to the models analyzed in [24–26], the proposed design is fundamentally different in that it dissipates energy via cyclic snap-through of the bi-stable element, as opposed to amplification of intrinsic damping. As discussed in detail in Section. 2.5, this results in a loss coefficient that is nearly frequency-independent and largely independent on the intrinsic material damping.

We first develop a rigorous analytical model of the 3-springs configuration, obtaining the equations that characterize its behavior under cyclic quasi-static loading. Subsequently, we adapt the model to a specific cellular material implementation, and present a simple mechanical analysis that clearly reveals the effect of the geometric parameters of the unit cell on the effective mechanical response of the material (stiffness, damping, isolation stress). The model is validated against finite elements analyses and experimental characterization, performed on a 3D printed prototype. Finally, we incorporate the validated model in an optimization framework to identify the geometric parameters that yield optimal combinations of effective Young's modulus and loss factor. Our simple implementation consists of a single material design that does not require external stabilization or pre-compression of buckled elements; these key features make it amenable to fabrication by virtually any additive manufacturing approach (from 3D printing to assembly and brazing) in a wide range of base materials (from polymers to metals) and at virtually any scale. We demonstrate that, when optimized, these architected materials exhibit extremely high combinations of Young's modulus and damping, far superior to those of the constituent material. Whereas our analysis is purely quasi-static, we show that the conclusions apply to dynamic loadings as well, as long as the frequency of oscillation is lower than the natural frequency of the internal degree of freedom, which can be tuned over wide ranges by geometrical scaling and material selection. The dynamic behavior of this system

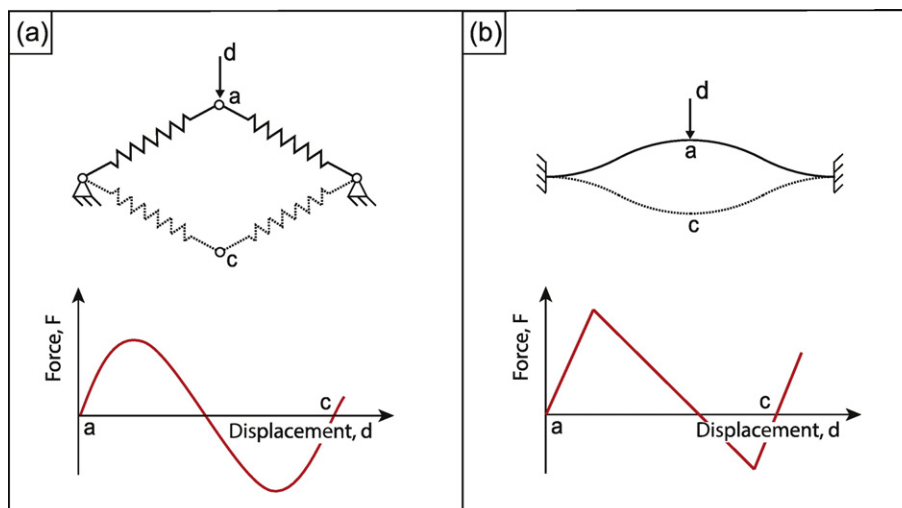


Fig. 1. Two examples of elements that can show negative stiffness, and their representative force-displacement behavior: (a) two pin joined springs arranged at an angle; (b) a sine shaped arch, with fixed end.

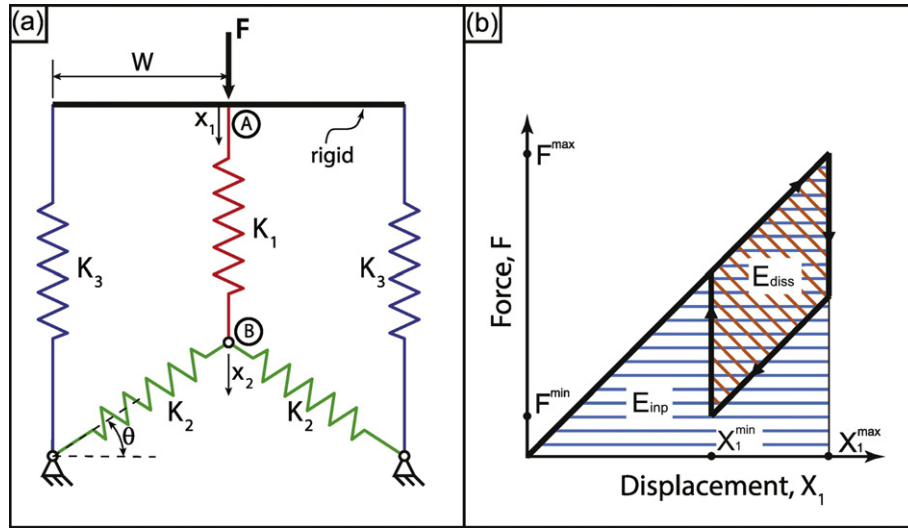


Fig. 2. (a) Schematic of the 3-springs configuration; (b) behavior of the 3-springs configuration under a loading-unloading cycle.

under frequencies that are comparable to the natural frequency of the internal degree of freedom is extremely complex and outside the scope of this work: it will be considered in future studies.

2. Mechanical response of negative stiffness-based cellular materials

2.1. Mechanical model of a 3-spring system

Consider the mechanical model in Fig. 2a. It consists of a linear spring of positive axial stiffness K_1 arranged in series with a non-linear element consisting of two linear springs of axial stiffness K_2 , pin jointed and oriented at an angle θ from the horizontal plane. Under vertical loads, the two springs of stiffness K_2 , arranged as described, form a non-linear element with the force-displacement behavior including a region of negative stiffness (Fig. 1a). The $K_1 - K_2$ system is arranged in parallel with another linear spring of axial stiffness K_3 . The springs K_1 and K_3 are assumed rigidly connected on their top nodes, with only one axial degree of freedom, and the bottom nodes of the springs K_2 are assumed pin jointed. The entire system, of width $2W$, is loaded with a cyclic vertical force F (assumed positive if pointing downwards). The displacement of point A is denoted X_1 , whereas the displacement of point B is denoted X_2 . We refer to this mechanical system as the ‘3-spring configuration’.

The qualitative behavior of the system under cyclic vertical loadings (Fig. 2b) is easily understood. When the system is compressed from its rest stage, the spring K_1 , if sufficiently compliant, will start accumulating strain until it can exert enough force to induce snap-through in the negative stiffness component, i.e. the assembly of 2 springs of stiffness K_2 ; after snap-through, the spring K_1 will release nearly all the strain; subsequently, when the load direction is reversed, a similar effect will occur, i.e. tensile stress build-up in the spring K_1 until snap through of the system of springs K_2 . Hence, the key to understand this hysteretic behavior is a detailed analysis of the mechanical response of the combination $K_1 - K_2$.

The effective static stiffness of the 3-spring configuration, K , is defined as the initial slope of the (F, X_1) curve; the effective loss factor, ψ , is defined as the ratio of the dissipated energy (E_{diss}) to the energy input (E_{inp}), i.e., $\psi = E_{diss}/(1/2 \cdot F^{max} \cdot X_1^{max})$.

To quantitatively analyze the behavior of the 3-spring configuration, we initially focus on the equilibrium between K_1 and K_2 , schematically represented in Fig. 3a. As before, we define X_1 the displacement of the top point (A) and X_2 as the displacement of the internal degree of freedom (B); F is the external force applied to the entire $K_1 - K_2$ system. If f_{K1} is the force in the spring K_1 and f_{K2} the vertical force in the system K_2 , equilibrium at point B implies: $f_{K2} - f_{K1} = 0$. This condition can be used to identify the force F and the displacement X_1 at which

snap-through occurs. This is schematically represented in Fig. 3b. As the entire system $K_1 - K_2$ is progressively compressed, the force $f_{K1} = K_1 \cdot (X_1 - X_2)$ develops in the spring K_1 . The vertical force in the system of springs of stiffness K_2 initially oriented at an angle θ_0 can be easily obtained by geometric considerations and expressed as:

$$\begin{aligned} f_{K2} &= 2K_2 \cdot (l_0 - l) \cdot \sin(\theta) \\ &= 2K_2 \cdot \left(\frac{W}{\cos\theta_0} - \sqrt{W^2 + (W \tan\theta_0 - X_2)^2} \right) \cdot \sin(\theta) \\ &= 2K_2 \cdot \left(\frac{W}{\cos\theta_0} - \sqrt{W^2 + (W \tan\theta_0 - X_2)^2} \right) \\ &\quad \times \sin\left(\tan^{-1}\left(\frac{W \tan\theta_0 - X_2}{W} \right) \right) \end{aligned} \quad (1)$$

where l and l_0 are the current and initial lengths of spring K_2 , respectively. These two forces are plotted as a function of X_2 in Fig. 3b, with f_{K1} represented as a straight line of slope $-K_1$, with intercept increasing upon loading. The equilibrium point is the intersection of f_{K1} and f_{K2} . This equilibrium is possible up to the tangency condition depicted in Fig. 3b (point i), after which sudden snap-through to point ii occurs. Upon unloading, the system remains stable up to point iii, after which it snaps to point iv. Hence, if we denote displacement and force at points i and iii as (X_2^+, f^+) and (X_2^-, f^-) , respectively, these critical values can be obtained as:

$$\begin{aligned} \left. \frac{dF}{dX_2} \right|_{X_2^+} &= -K_1 f^+ = f_{K2} \quad (X_2 = X_2^+) \quad X_2^+ \in [0, W \tan\theta_0] \\ &\text{and} \\ \left. \frac{dF}{dX_2} \right|_{X_2^-} &= -K_1 f^- = f_{K2} \quad (X_2 = X_2^-) \quad X_2^- \in [W \tan\theta_0, 2W \tan\theta_0] \end{aligned} \quad (2)$$

As f_{K2} is antisymmetric with respect to $X_2 = W \tan\theta_0$, clearly we have: $f^- = -f^+$, and $X_2^- = 2W \tan\theta_0 - X_2^+$. We can plot the behavior of the entire $K_1 - K_2$ system in the $F - X_1$ domain (Fig. 3c): X_1^{max} and X_1^{min} can be easily found as:

$$K_1 \cdot (X_1^{max} - X_2^+) = f^+ \Rightarrow X_1^{max} = X_2^+ + \frac{f^+}{K_1} \quad (3)$$

$$K_1 \cdot (X_1^{min} - X_2^-) = f^- \Rightarrow X_1^{min} = X_2^- + \frac{f^-}{K_1} \quad (4)$$

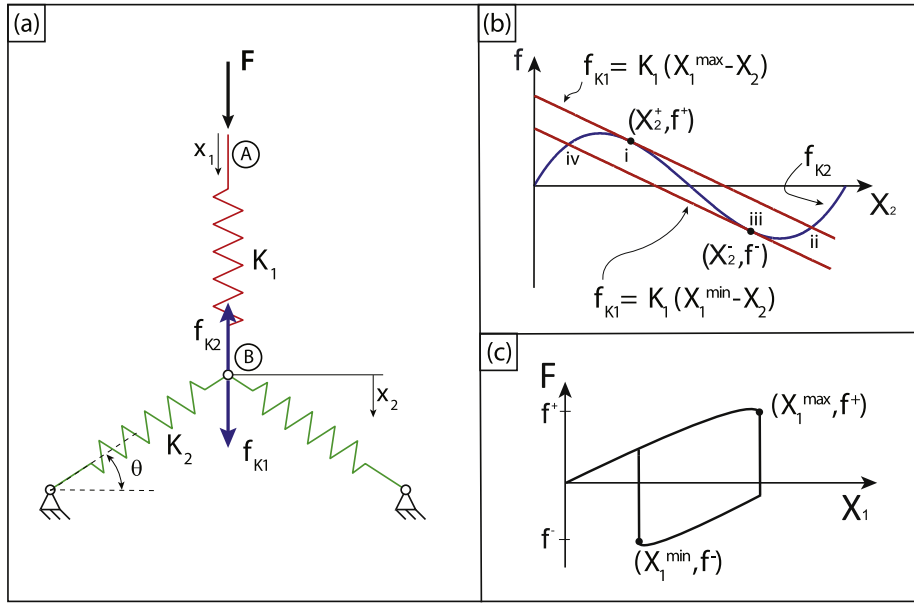


Fig. 3. Analysis of the K_1 – K_2 equilibrium. (a) Sketch of the elements and definition of variables; (b) force-displacement diagrams for the equilibrium of point B: f_{K_1} is in blue, f_{K_2} is in red; (c) force-displacement curve for the entire 2-spring system (equilibrium of point A).

Notice that the loading curve in Fig. 3c is not exactly a straight line, due to the shape of the load–displacement curve of K_2 . However, it is generally very close to a straight line. The addition of the spring K_3 to the 3-spring system has a simple stiffening effect, i.e.:

$$F^{\max} = f^+ + 2 \cdot K_3 \cdot X_1^{\max} \quad (5)$$

$$F^{\min} = f^- + 2 \cdot K_3 \cdot X_1^{\min} \quad (6)$$

resulting in the overall mechanical response of the entire 3-spring system depicted in Fig. 2b.

From Eq. (2) and Fig. 3b, we can extract a necessary condition for hysteretic behavior, i.e.: $K_1 < |dF/dX_2|_{x_2 = W \tan \theta_0}$; this imposes that the spring K_1 must be more compliant than the maximum stiffness of the system K_2 in its negative stiffness region.

For most cyclic load applications, we want to request that the load–displacement behavior be recoverable, i.e., that the force F^{\min} be positive. This condition is easily expressed as $F^{\min} = f^- + 2 \cdot K_3 \cdot X_1^{\min} > 0$.

Finally, we can express the dissipated energy as:

$$E_{diss} = \left((F^{\max} - F^{\min}) (X_1^{\max} - X_1^{\min}) - (X_1^{\max} - X_1^{\min})^2 \frac{F^{\max}}{X_1^{\max}} \right) \quad (7)$$

$$\equiv \left((f^+ - f^-) (X_1^{\max} - X_1^{\min}) - (X_1^{\max} - X_1^{\min})^2 \frac{F^{\max}}{X_1^{\max}} \right)$$

The loss factor can then be expressed as:

$$\psi = \frac{E_{diss}}{\frac{1}{2} F^{\max} \cdot X_1^{\max}} \quad (8)$$

If we assume an architected material with unit cell schematically depicted in Fig. 2a, the effective Young's modulus of the material can be written as:

$$\bar{E} = \frac{F^{\max}/2WD}{X_1^{\max}/H} = \frac{F^{\max}}{X_1^{\max}} \cdot \frac{H}{2WD} = \frac{f^+ + 2 \cdot K_3 \cdot X_1^{\max}}{X_1^{\max}} \cdot \frac{H}{2WD} \quad (9)$$

where W , H and D represent the semi-width, height and depth of the unit cell.

The product of the Young's modulus and the loss factor is a key figure of merit for stiff dampers, i.e.:

$$\Pi = \bar{E} \cdot \psi = \frac{F^{\max}}{X_1^{\max}} \cdot \frac{H}{2WD} \cdot \frac{E_{diss}}{\frac{1}{2} F^{\max} \cdot X_1^{\max}} = \frac{2 \cdot E_{diss}}{(X_1^{\max})^2 \cdot L} \cdot \frac{H}{2WD} \quad (10)$$

This analytical model can be graphically expressed in the form of design maps, visualizing the influence of all geometric parameters on the energy dissipation. The geometric variables are non-dimensionalized a K_2/K_1 , K_3/K_1 , X_1/W , X_2/W and θ_0 . Fig. 4 presents contour plots of the normalized figure of merit, $\bar{\Pi} = \bar{E} \cdot \psi \cdot 2WD/HK_1$, as a function of K_3/K_1 and K_2/K_1 , for four different values of the initial angle θ_0 . The dashed areas in the plots correspond to conditions in which F^{\min} is negative, resulting in non-recoverable behavior.

From these maps, the following important observations can be extracted:

- (i) An increase in the geometric parameter K_2/K_1 always results in increased values of the figure of merit, Π .
- (ii) The geometric parameter K_3/K_1 does not significantly affect the magnitude of the figure of merit; this is because while the effective Young's modulus of the system is directly proportional to K_3/K_1 , the loss factor is inversely proportional to the same geometric parameter (this conclusion can be derived from Equations (10) and (7)), and the two effects approximately cancel out.
- (iii) As the initial angle θ_0 is increased, the vertical force exerted by the spring system K_2 increases, and hence the parameter K_2/K_1 has to be reduced in order to achieve the same value of the figure of merit, Π . An important implication is that the maximum value of K_2/K_1 that ensures a recoverable system decreases as θ_0 is increased.
- (iv) Recoverability is strongly affected by the parameter K_3/K_1 : the smaller this parameter, the smaller the recoverability range.
- (v) The maximum values of the figure of merit Π are achieved for values of the parameter K_2/K_1 that are at the cusp of non-recoverability. In other words, near-optimal recoverable systems are very difficult to design, as any small geometric defects might result in loss of recoverability.

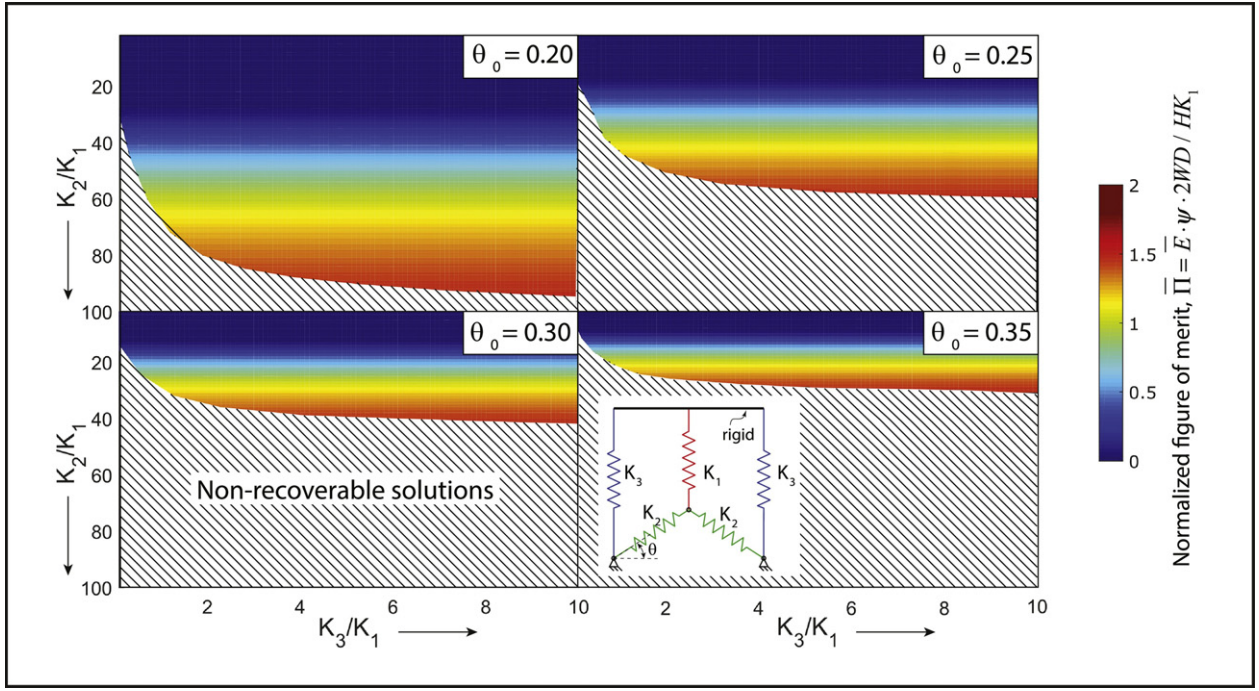


Fig. 4. Design maps for the 3-spring configuration, illustrating contours of the normalized figure of merit ($\bar{\Pi} = \bar{E} \cdot \psi \cdot 2WD / (HK_1)$) versus the ratios K_2/K_1 , and K_3/K_1 , for different values of the initial angle θ_0 . The dashed areas represent irrecoverable behavior.

- (vi) Increasing the initial angle θ_0 does not necessary imply an increase in the figure of merit, Π . This counterintuitive result can be explained as follows: whereas increasing θ_0 clearly increases the dissipated energy, it also implies that more displacement, hence more energy, has to be applied to result in hysteretic behavior; the two effects roughly cancel out, and as a result θ_0 has a small effect on the maximum achievable value of the figure of merit, Π .

We conclude this section by emphasizing that these important observations are general and apply to any physical implementation of a cellular material (or a structure) that is mechanically represented by the 3-spring configuration depicted in Fig. 2a. All these conclusions are very useful in informing the choice of a practical implementation with near-optimal performance.

2.2. Mechanical model of a cellular material implementation

In this section, we propose and characterize a cellular material implementation of the 3-spring model described in the previous section. A schematic drawing of the unit cell and the multi-cell material, together with a 3D printed unit cell are shown in Fig. 5. To enable simple fabrication in a single material system without the need for joints and/or complex assembly, all springs are implemented as arches. The shapes of the semicircular arches implementing the springs K_1 and K_3 are chosen to allow large strains in the linear regime without yielding or buckling. Clearly, this poses a limit on the stiffness of the entire system, as both springs are bending-dominated. The implications of this decision are detailed in the following sections. The K_2 two-spring assembly is implemented as a double arch, as opposed to the more common pre-buckled beam; differently from a pre-buckled beam, the arch does not require external pre-compression, thus dramatically simplifying the fabrication of a cellular material design; the choice of a double arch as opposed to a single arch ensures symmetric snap-through, without rotation of the central point, hence avoiding less snappy anti-symmetric modes.

The behavior of an arch under compression is qualitatively similar, but not quantitatively identical, to the two-spring K_2 model analyzed in Section. 2.1. A mechanical model of the $K_1 - K_2$ system with the arch implementation is depicted in Fig. 6. The behavior of an arch (deforming via mode 3 snap-through instability) was derived in [28]. The key difference relative to the 2-spring system is that the force-displacement curve for the arch has a sharp transition between positive and negative stiffness regions. Hence we simply have: $X_2^+ = d_{top}$, $X_2^- = d_{bot}$, $f^+ = 2 \cdot f_{top}$ and $f^- = 2 \cdot f_{bot}$ (see Fig. 6b), where the factor 2 in the force terms results from the choice of a 2-arch spring. Equilibrium of the $K_1 - K_2$ system imposes:

$$2 \cdot K_1 \cdot (X_1^{\max} - d_{top}) = 2 \cdot f_{top} \quad (11)$$

$$2 \cdot K_1 \cdot (X_1^{\min} - d_{bot}) = 2 \cdot f_{bot} \quad (12)$$

The factor of 2 reflects the presence of two springs. From Eqs. (11) and (12) we readily obtain:

$$X_1^{\max} = d_{top} + \frac{2 \cdot f_{top}}{2 \cdot K_1} \quad (13)$$

$$X_1^{\min} = d_{bot} + \frac{2 \cdot f_{bot}}{2 \cdot K_1} \quad (14)$$

The condition that ensures hysteretic behavior in this case can be expressed as: $-K_1 \geq (f_{bot} - f_{top}) / (d_{bot} - d_{top})$; in other words, K_1 has to be more compliant than the absolute value of the negative stiffness of the double arch.

If we now introduce the additional positive stiffness springs K_3 , the maximum and minimum forces in the system are given by:

$$F^{\max} = 2 \cdot f_{top} + 4 \cdot K_3 \cdot X_1^{\max} \quad (15)$$

$$F^{\min} = 2 \cdot f_{bot} + 4 \cdot K_3 \cdot X_1^{\min} \quad (16)$$

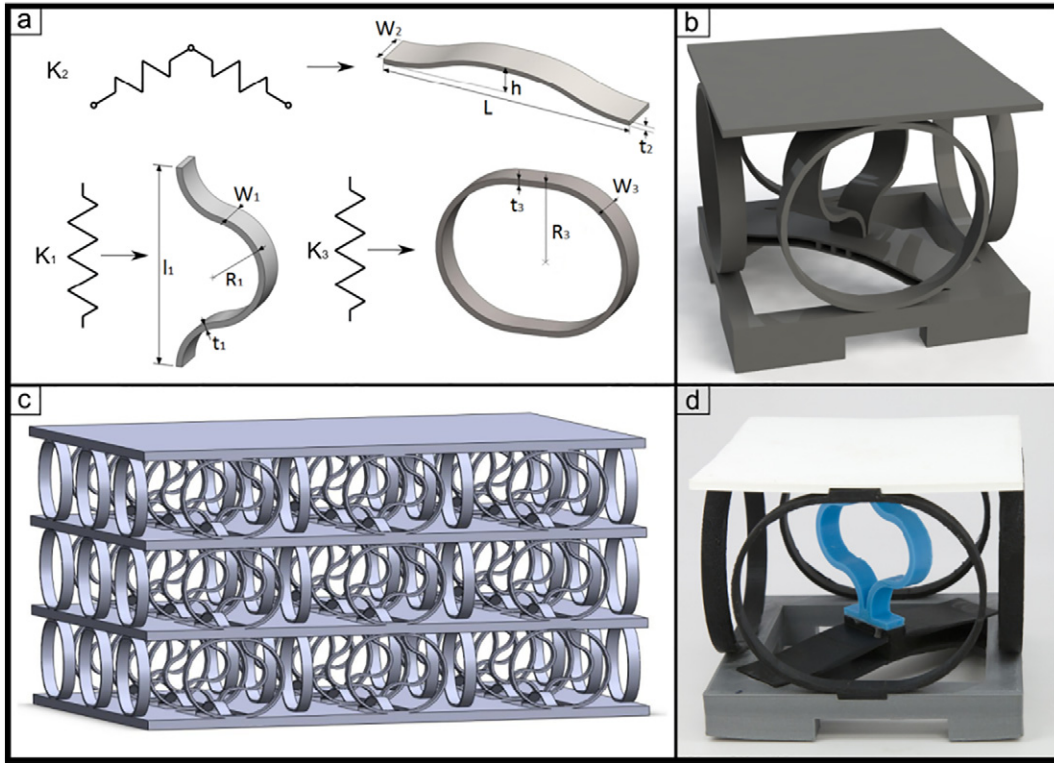


Fig. 5. Architected material implementation of the 3-spring configuration depicted in Fig. 2. (a) Geometry of each spring element; (b) CAD model of a unit cell; (c) CAD model of a three-dimensional lattice; (d) physical implementation of a unit cell, produced by Fused Deposition Modelling.

The dissipated energy can be expressed as:

$$E_{diss} = \left((F^{max} - F^{min}) (X_1^{max} - X_1^{min}) - (X_1^{max} - X_1^{min})^2 \frac{F^{max}}{X_1^{max}} \right) \quad (17)$$

$$\equiv \left(2 \cdot (f_{top} - f_{bot}) (X_1^{max} - X_1^{min}) - (X_1^{max} - X_1^{min})^2 \frac{F^{max}}{X_1^{max}} \right)$$

with the loss factor following as: $\psi_l = E_{diss} / (F^{max} \cdot X_1^{max} / 2)$.

The expressions for the effective Young's modulus is given by:

$$\bar{E} = \frac{F^{max} / L^2}{X_1^{max} / L} = \frac{F^{max}}{X_1^{max} \cdot L} = \frac{2 \cdot f_{top} + 4 \cdot K_3 \cdot X_1^{max}}{X_1^{max} \cdot L} \quad (18)$$

with L the size of the cubic unit cell.

Once again, we define the key figure of merit for our architected material as the product of the Young's modulus and the loss factor of its unit cell, i.e., $\Pi = \bar{E} \cdot \psi$.

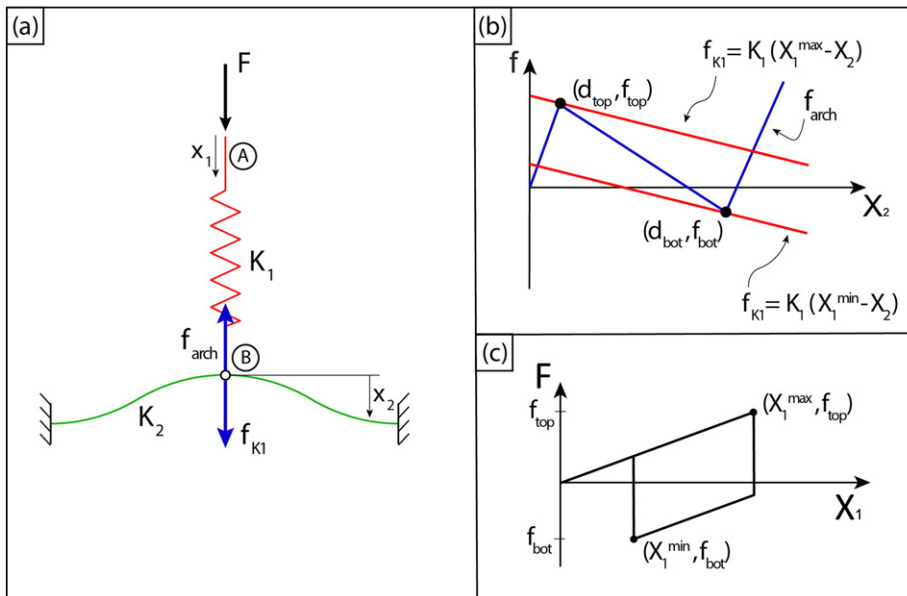


Fig. 6. Analysis of the $K_1 - K_2$ equilibrium for an arch implementation of K_2 . (a) Sketch of the elements and definition of variables; (b) force-displacement diagrams for the equilibrium of point B: f_{K1} is in blue, f_{arch} is in red; (c) force-displacement curve for the entire 2-spring system (equilibrium of point A).

We now need to express the spring stiffness K_1 , K_2 and K_3 as a function of the geometric parameters of its implementations. Details are provided in Appendix A. With reference to the geometric variables defined in Fig. 5a, the results are:

$$K_1 = aEW_1 \left(\frac{t_1}{l_1}\right)^3 \quad (19)$$

$$K_3 = bEW_3 \left(\frac{t_3}{R_3}\right)^3 \quad (20)$$

with E the Young's modulus of the parent material, $a = 1.4$ and $b = 0.46$.

The mechanical response of the K_2 arch is fully characterized by two force values (f_{top} and f_{bot}) and two displacement values (d_{top} and d_{bot}). These are given by [28]:

$$\begin{aligned} f_{top} &= \left(8\pi^4 - 6\pi^4 \frac{d_{top}}{h}\right) \frac{E_s h t_2^3 W_2}{12L^3} \\ f_{bot} &= \left(8\pi^4 - 6\pi^4 \frac{d_{bot}}{h}\right) \frac{E_s h t_2^3 W_2}{12L^3} \\ d_{top} &= h \left(1 - \sqrt{1 - \frac{16}{3(h/t_2)^2}}\right) \\ d_{bot} &= h \left(1 + \sqrt{1 - \frac{16}{3(h/t_2)^2}}\right) \end{aligned} \quad (21)$$

For proper operation, we must clearly impose that the material remain elastic over the entire cycle, up to the limit force f_{top} . Imposing this condition requires an expression for the maximum stress in each spring element as a function of the displacement X_1 . Refer to Appendix A for details. For spring elements K_1 and K_3 the maximum stresses are given by:

$$\sigma_1^{\max} = cE_s \frac{t_1}{l_1^2} (X_1 - X_2) + dE_s \frac{t_1^2}{l_1^3} (X_1 - X_2) \quad (22)$$

$$\sigma_3^{\max} = eE_s \frac{t_3}{R_3^2} X_1 \quad (23)$$

with $c = 2.1$, $d = 1.4$ and $e = 3/\pi$.

The maximum stress in the arch K_2 is reached during snap-through and can be expressed as [28]:

$$\sigma_2^{\max} = \pi^2 E_s \frac{t_2 h}{L^2} \left(2 + \frac{4t_2}{3h}\right) \quad (24)$$

The conditions that all stresses remain below the yield strength of the material will be imposed as constraints in the optimization algorithm, to ensure that all springs remain elastic over the entire range of motion.

2.3. Numerical modeling and verification

In order to verify the simple analytical model discussed in the previous section, a Finite Elements simulation is performed with the commercial software Abaqus. A unit cell conceptually identical to that in Fig. 5b is modeled with shell elements (S4R). To simplify meshing, the K_3 spring is modeled as two loops, as opposed as the four loops shown in Fig. 5b; similarly, the K_2 double arch depicted in Fig. 5b is modeled as a single arch and rotated. The widths and thicknesses of all the elements are properly adjusted to result in the desired stiffness. The top and bottom frames of the unit cell are not explicitly modeled; rather, all springs are fully clamped at the top and bottom sides. The top side is uniformly displaced in the negative vertical direction, resulting in uniaxial compression. Capturing the large instabilities that occur upon snap-through is a considerable challenge for traditional

quasi-static Finite Elements algorithms. Although dynamic explicit algorithms could in principle be used, their conditional stability requires extremely time-intensive simulations to model deformation rates that are slow enough to approximate the quasi-static response. To address these challenges, we use the Riks algorithm, a quasi-static numerical scheme that was specifically designed to model post-buckling response. In this algorithm, both the load and displacement increments at each iteration are treated as variables (unlike in load or displacement controlled static simulations). Therefore, another quantity must be used to measure the progress of the solution: Abaqus uses the "arc length", which is defined in order to follow the tangent stiffness of the system extracted from the previous iteration. Upon snap-through, the load suddenly drops and the algorithm automatically inverts the direction of the displacement increment in order to maintain convergence. During this process, energy is artificially dissipated. When the system reaches stability again, the displacement increment returns to the original direction and the loading cycle continues. A similar phenomenon occurs upon unloading. In order to ensure convergence, we limit the arc length in the range $[10^{-100} \text{ mm} - 0.08 \text{ mm}]$, with the maximum number of iterations set to 10^7 .

The geometry of the unit cell is chosen as follows:

$$\begin{aligned} K_1 &\begin{cases} t_1 = 2.1 \text{ mm} \\ l_1 = 54.2 \text{ mm} \\ W_1 = 9.7 \text{ mm} \end{cases} \\ K_2 &\begin{cases} t_2 = 1.1 \text{ mm} \\ h_2 = 5.4 \text{ mm} \\ W_2 = 30 \text{ mm} \\ L_2 = 100 \text{ mm} \end{cases} \\ K_3 &\begin{cases} t_3 = 2.6 \text{ mm} \\ R_3 = 39.8 \text{ mm} \\ W_3 = 10.2 \text{ mm} \end{cases} \end{aligned} \quad (25)$$

The material is modeled as linear elastic, with Young's modulus, $E = 1740 \text{ MPa}$ and mass density, $\rho = 1100 \text{ kg/m}^3$. These values are representative of acrylonitrile butadiene styrene (ABS) printed in a Flashforge Creator Pro Fused Deposition Modeling machine, with fiber orientation along the loading direction (see Appendix B). As the unit cell is designed to undergo snap-through without yielding, no plastic properties are defined.

The load-displacement curve for the unit cell obtained by the Finite Elements simulation is depicted in Fig. 7, alongside the analytical prediction. Images of the deformed mesh with Von Mises stress contours at three points in the simulation ((1) along the loading path, (2) immediately before snap-through, and (3) after snap-through) are shown in the insets. Notice that the numerical load-displacement curve has a S-shape. This is characteristic of the Riks post-buckling analysis; although those are equilibrium positions, there are unattainable in a load or displacement controlled experiment. A displacement controlled loading-unloading experiment would result in a sudden load decrease at snap-through upon loading, and a sudden load increase at snap-through upon unloading (dashed vertical lines).

Note that the FE simulation agrees quite well with the analytical prediction in terms of stiffness, shape/size of the hysteresis cycle, and loads at snap-through events. The displacement width of the hysteresis cycle is slightly overpredicted by the analytical model. This discrepancy is primarily attributed to an overestimation of the rigidity of the torsional boundary conditions for the arch. Overall, though, this simulation verifies the accuracy of the analytical model.

2.4. Fabrication and experimental validation

A unit cell sample with the topology represented in Fig. 5b, and geometry notionally identical to that employed in the FE analyses, is additively manufactured in the polymer acrylonitrile butadiene styrene (ABS) via Fused Deposition Modeling (FDM). A Flashforge Creator Pro

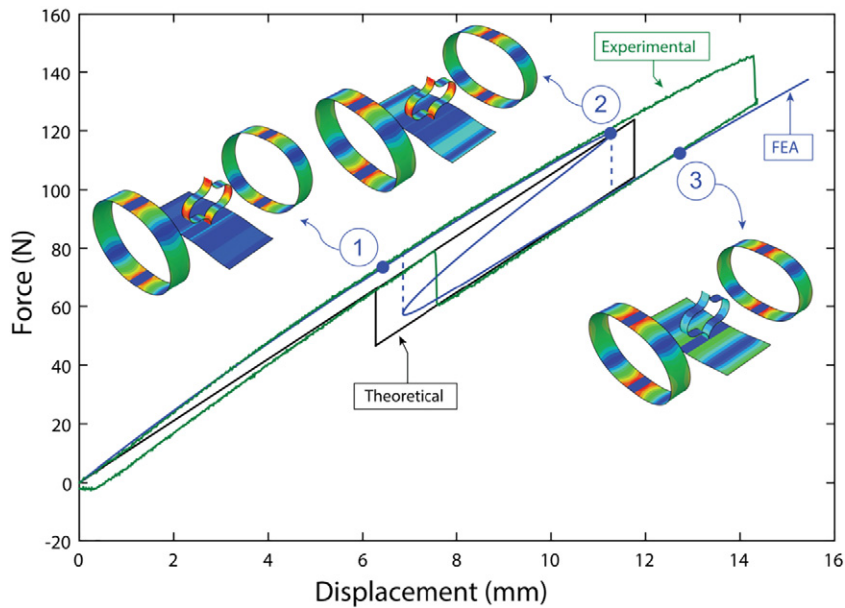


Fig. 7. Force-displacement curve for the architected material implementation of the 3-spring configuration: analytical model in black, numerical model in blue, and experimental results in green. The insets show displacement and equivalent stress contours at three specific points in the numerical simulation.

is used for all prints. The three spring elements are printed separately, to ensure that the filaments of ABS be aligned with the direction of maximum loading for each spring. The fully assembled unit cell is shown in Fig. 5d (different colors are used for visual clarity, although the base material is the same throughout).

The mechanical response of the base material is characterized by uniaxial loading of a dog bone sample of ABS printed with filaments along the loading direction: elastic modulus and yield strength of the base material are extracted from the uniaxial stress-strain curve (see Appendix B for details).

The fully assembled unit cell is tested in uniaxial compression under displacement control. A displacement of 15 mm is applied at constant rate of 0.1 mm/s; this rate is chosen to be faster than the rate used in the tensile test of the parent material (Appendix B), in order to minimize viscoelastic effects. Soon after the occurrence of snap-through, the displacement direction is reversed and the compression platen is brought back to the original position.

The load-displacement curve for the whole cycle is depicted in Fig. 7, alongside the analytical and numerical predictions. The following observations can be made: (a) The stiffness of the sample is perfectly captured by the numerical model. Both experimental and numerical curves show a decrease in slope upon loading (which is not predicted by the analytical model); in principle, this could be due to viscoelastic behavior of the polymer or geometric non linearities. However, as the numerical model assumes linear elastic behavior with constant Young's modulus and no time dependence, we conclude that this feature is associated with geometric non-linearities, which are well captured by the numerical model. (b) The magnitude of the load drop upon snap-through (and subsequent load increase upon reverse snap-through) are well captured by the models. (c) The area of the hysteresis cycle (energy dissipation) is under-predicted by the models, by ~16%. This is attributed to the viscoelastic behavior of the polymer, whereby some amount of energy is dissipated in the polymeric material itself. (d) The displacements at which snap-through occurs upon loading and unloading are under-predicted by the models, by ~17%. This is attributed to imperfect fit among the various components and general manufacturing imperfections.

Overall, the experiment on a single unit cell validates the analytical model to a degree that is more than adequate for optimal design studies. In the next section, we will investigate the optimal design of an

architected material based on this architecture with exceptional combinations of stiffness and energy dissipation.

2.5. Upper bound on excitation frequency

In traditional damping materials (e.g., viscoelastic solids), the energy loss characteristics are frequency dependent, due to the viscous nature of the loss mechanism. One very important aspect of the bi-stable system investigated in this work is that energy loss is to first order not frequency dependent, but rather amplitude dependent. The amplitude sensitivity arises due to the bi-stability of the system and the existence of a critical load or displacement that triggers snap-through. For the envisioned lattice material, the sensitivity to stroke and amplitude strongly depend on the choice of the design parameters, i.e. different combinations of elastic constants, as well as interactions between neighboring elements. Such interaction effects are out of scope for this paper, although they could be studied with the mechanical analysis presented herein.

The frequency-independence of the loss coefficient in the bi-stable system analyzed in this work is subject to a very important caveat: the forcing frequency must be much lower than the natural frequency of oscillation of the internal degree of freedom. As long as this condition is met, the energy stored in the elastic system immediately prior to snap-through is quickly dissipated by high frequency vibrations of the internal degree of freedom, which strongly enhance any loss mechanisms present in the system (e.g., viscoelastic damping within the material, viscous damping by the air, structural damping at the connectors, etc...). This results in the 'clean' hysteresis cycles seen in Fig. 7. If the forcing frequency of oscillation approaches the natural frequency of the internal degree of freedom (henceforth denoted as f_r), a much more complex regime ensues, for which the quasi-static analysis presented in this work is no longer adequate (although substantial energy dissipation is still possible). Although certainly interesting both scientifically and technologically, a detailed analysis of this complex regime is far outside of the scope of this work. The implication is that the quasi-static results presented in this work are (i) essentially frequency independent and (ii) valid up to a critical frequency, f_r . We now proceed to estimate this critical frequency.

The dynamics of the internal degree of freedom are determined by the elastic constants and mass characteristics of the elements. Before

and after a snap-through event, the internal degree of freedom has a dynamic response that can be represented by a lumped model that includes the effective stiffness of the upper spring (K_1), the effective stiffness of the arch (K_2) and a lumped effective mass in the center. This element then has a resonant frequency given by:

$$f_r = \frac{1}{2\pi} \sqrt{\frac{K_1 + K_2}{m_{eff}}} \quad \text{and} \quad m_{eff} = \alpha_1 m_1 + \alpha_2 m_2 \quad \text{and} \quad 0 < \alpha < 1 \quad (26)$$

where K_1 is given by Eq. (19), K_2 is given by Eq. (21), m_1 and m_2 are the masses of the two springs, and α_1 , α_2 are non-dimensional geometric parameters of order 1. If the states are similar before and after snap through, then the impulse in both directions will create an oscillation about the mean position at this frequency. The oscillation will be damped down by the intrinsic and extrinsic loss mechanisms described above.

A realistic lower bound for the resonant frequency can be obtained by assuming $\alpha_1 = \alpha_2 = 1$ in Eq. (26). With this assumption and the geometric dimensions and materials properties reported above, the resonant frequency of the internal degree of freedom for the prototype depicted in Fig. 5d can be estimated as 407 Hz (see Eqs. (19) and (21)). This frequency is over 5 orders of magnitude higher than the exciting frequency (~0.003 Hz), which explains why the hysteresis loops in Fig. 7 show almost perfectly sharp snap-through events. A finite elements analysis of the $K_1 - K_2$ system was also conducted to verify the assumptions made in estimating the effective mass in Eq. (26). The FE results provide a resonant frequency of 500 Hz, consistent with values of $\alpha_1 = \alpha_2 = 0.66$. Hence the simplified analytical model is overly conservative by ~20%.

Importantly, Eq. (26) can be used to estimate the effect of geometric scaling and materials selection on the natural frequency of the internal degree of freedom, and hence the maximum operating frequency of the architected material. If we scale all dimensions by a factor β (i.e., $t_1 = \beta \cdot t_1^0$; $t_2 = \beta \cdot t_2^0$; $W_1 = \beta \cdot W_1^0$; $W_2 = \beta \cdot W_2^0$..., where $t_1^0, t_2^0, W_1^0, W_2^0$... are the original dimensions), then simple scaling arguments show that all masses scale as β^3 , whereas all stiffness scale as β . The implication from Eq. (26) is that the resonant frequency of the internal degree of freedom scales as $1/\beta$. Similarly, if we replace our material with density ρ_0 and modulus E_0 with a different material with density ρ and modulus E , the resonant frequency of the internal degree of freedom changes by $\sqrt{E/\rho} / \sqrt{E_0/\rho_0}$. As an example, if we fabricate our device in aluminum with a unit cell size of 1 cm, the maximum operating frequency rises to ~11 kHz. For many applications, this value is well above the expected usage conditions of the material. Clearly, micro-scale systems would result in much higher maximum operating frequencies.

3. Optimal design

3.1. Statement of the optimization problem

We seek to identify the optimal dimensions for the architected material schematically represented in Fig. 5 for maximum combinations of stiffness and loss factor. Specifically, the objective function will be the figure of merit, $\Pi = \bar{E} \cdot \psi$ introduced in Section. 2. We assume that the unit cell has external dimensions $L \times L \times L$, and the design variables are the dimensions $t_1, l_1, W_1, t_2, h, W_2, t_3, R_3, W_3$ (see Fig. 5a for variable definition). Two constraints need to be imposed: (i) none of the structural elements are allowed to yield during the entire loading-unloading cycle, and (ii) the unit cell is required to be recoverable, i.e., it must return to its initial configuration upon unloading. Solving this problem numerically as stated presents numerous computation challenges. In particular, infinitely many combinations of the geometric variables exist that result in the optimal configuration. As an example, consider the spring K_1 , which is defined by 3 geometric variables (t_1, l_1, W_1): once the optimal value of the stiffness K_1 is determined, and the

condition of no yielding, i.e., $\sigma_1^{\max}(t_1, l_1) < \sigma_y$ is imposed, infinitely many combinations of (t_1, l_1, W_1) exist that satisfy all conditions. The same is true for other springs. Besides, each value of the objective function Π can be obtained by infinite combinations of \bar{E} and ψ . All this results in an infinite set of optimal solutions, which make this optimization problem challenging to solve numerically. Furthermore, the no yielding conditions are non-linear (see Eqs. (22)–(24)), which results in significant computational cost.

To make the numerical optimization more tractable, we make two important modifications to the problem statement:

- (1) We treat the stiffness of the spring K_1 as an independent variable (defined within a reasonable range), so that the values of its geometric parameters (t_1, l_1, W_1) do not enter the optimization problem. Once the optimal value of K_1 is identified by the optimizer, we apply the non-linear no yielding condition to the element K_1 to identify a suitable set of geometric parameters. Clearly, the advantages of this approach are two-fold: first, we reduce the number of variables from 6 to 4 and eliminate a nonlinear constraint, thus reducing the computational cost of the optimization algorithm; second, we eliminate the infinite set of local optima related to the under-determination of the geometry of K_1 .
- (2) Rather than using the figure of merit, $\Pi = \bar{E} \cdot \psi$, directly as the objective function, we sweep the Young's modulus of the cell, \bar{E} , within a prescribed range, and for every value of \bar{E} we solve for the geometry that maximizes ψ . As K_3 (and hence its geometric variables t_3, R_3, W_3) only affect \bar{E} (and not ψ), this approach further reduces the number of variables.

Hence, the statement of the optimization problem is the following: For any given value of \bar{E} within a prescribed range, we find the values of the variables K_1, t_2, h, W_2 that maximize ψ , subjected to the following constraints: (a) no yielding of the arch (spring K_2); (b) recoverability under a compression cycle, i.e. $F^{\min} > 0$; (c) $h/t_2 > 2.31$ (a condition reported in [28] to ensure vertical symmetry in the buckling mode of the arch, important for energy dissipation). The yield strain and Young's modulus of the parent material, ε_y and E_s , and the overall size of the unit cell, L , are assumed fixed parameters. As we want to ensure that the optimal geometry could be 3D printed with a FlashForge Creator Pro, we choose the range for the geometric parameters within the resolution and range of the machine, i.e.: $t_2 \geq 0.4\text{mm}$ and $1\text{mm} \leq W_2 \leq 30\text{mm}$. The feasible range of K_1 is chosen as $4 \cdot 10^{-6}\text{N/mm} \leq K_1 \leq 10\text{N/mm}$.

The Active Set algorithm of Matlab is used for all optimization studies. Unlike most non-linear optimization tools, this algorithm estimates a subset of constraints to watch while searching for the solution, rather than imposing all constraints and bounds at every iteration. The gradients of the objective function and constraints are approximated using a forward difference scheme. The function tolerance has been set to 10^{-6} , the constraint tolerances to 10^{-12} , and the maximum number of iterations to 10^4 . These parameters offered excellent convergence for our problem, while providing solutions in agreement with all constraints.

This optimization process is repeated for three different values of yield strain of the parent material ($\varepsilon_y = [0.005, 0.01, 0.02]$). For each value of ε_y , an appropriate range for \bar{E}/E_s is chosen, with the upper bound limited by the no yielding constraint, and the lower bound limited by manufacturability constraints. For $\varepsilon_y = 0.005$, $\bar{E}/E_s \in [3 \cdot 10^{-5}, 4 \cdot 10^{-7}]$; for $\varepsilon_y = 0.01$, $\bar{E}/E_s \in [10^{-4}, 4 \cdot 10^{-7}]$; and for $\varepsilon_y = 0.02$, $\bar{E}/E_s \in [3 \cdot 10^{-4}, 4 \cdot 10^{-7}]$. To ensure that the algorithm converge to a global optimum, each optimization study is repeated for 6 different values of the initial guesses (5 randomly chosen values + the solution obtained for the previous value of \bar{E}/E_s) and the independence of the solution on the choice of initial guess is verified.

3.2. Performance of optimal designs

The optimal results are shown in Fig. 8, plotting the optimal combinations of Young's modulus of the architected material (here normalized by the Young's modulus of the parent material) and the loss factor, ψ . The scale is logarithmic on both axes. Recall that the product of Young's modulus and loss factor represent our figure of merit, Π . The three curves represent three different values of the yield strain of the parent material, ε_y . A number of important considerations can be made:

- (i) The maximum value of the loss factor that can be achieved with this design is $\psi = 0.5$. The explanation is simple: we have defined ψ as the ratio of the area of the hysteresis loop to the area under the loading path, and we have constrained the system to be reversible (i.e., all the hysteresis loop must be contained in the positive force quadrant). Clearly, the maximum area of a rhomboid (area of the hysteresis loop) that fits inside a triangle (area under the loading curve) is one half of the area of the triangle. It is important to realize that different publications utilize different definition for the loss factor; as a result, alternative designs in other publications might have vastly different values of the optimal loss factors. The reader is encouraged to ensure consistent definitions, before attempting to compare optimal results.
- (ii) All the optimal curves in Fig. 8 are clearly bi-linear, composed of a line of slope -1 and a vertical line at $\psi = 0.5$. All points in the -1 slope range have the same values of the figure of merit $\Pi = \bar{E} \cdot \psi$. The explanation for this characteristic is illustrated in the insets in Fig. 8, where load-displacement curves are produced for three points on the optimal design curve: point 1 is in the -1 slope range, point 2 is at the intersection of the diagonal and vertical lines, and point 3 is in the vertical slope range. For all points on the -1 slope line, the no-yielding-of-the- K_2 -element constraint is active; hence, all the designs in that range have the same dimensions for the K_1 and K_2 springs, and thus the same value of $\Pi = \bar{E} \cdot \psi$ (see point 1 as an example). As the Young's modulus, \bar{E} , is decreased, K_3 decreases while the area of the hysteresis loop is maintained constant, resulting in an increase in the loss factor (ratio of the dissipated energy to the applied energy).

When F^{\min} hits the x axis (point 2), we can no longer reduce K_3 while maintaining the area of the hysteresis loop constant; this activates the constraint $F^{\min} \geq 0$; from this point on, as we keep decreasing K_3 (proportional to the Young's modulus of the material), the area of the hysteresis loop is reduced while the loss factor remains constant at 0.5. Point 3 is representative of this regime. If the Young's modulus of the architected material is reduced beyond point 2, the solution becomes sub-optimal, i.e. a solution can be found with the same value of the loss factor and a higher values of the Young's modulus.

- (iii) The yield strain of the parent material has a marked positive effect on the figure of merit.
- (iv) With our choice of constituent materials and geometry, the maximum value of the figure of merit $\Pi = \bar{E} \cdot \psi$ is $5 \cdot 10^{-5} \cdot E_s$, with E_s the Young's modulus of the parent material.

If we recall the design maps related for the generic 3-springs configuration (Fig. 4), we had observed that the figure of merit is independent on the value of K_3/K_1 , as long as K_3/K_1 is sufficiently large. As K_3/K_1 is reduced while K_2/K_1 is maintained constant, the design eventually becomes irrecoverable. If one insists on reducing K_3/K_1 further beyond this critical value, K_2/K_1 must be reduced at the same time, in order to maintain recoverability. The relationship between those findings and the optimal design curve discussed in this section are clearly illustrated in Fig. 9: Point A is within a recoverable design range. As the Young's modulus of the architected material is reduced between point A and point B, the system maintains a constant value of the figure of merit. At point B, the boundary delimiting the recoverability range is met; as the modulus is decreased further, from point B to point C, the optimal designs skirt the boundary of the recoverability range, and the solutions become sub-optimal.

One further remark can be made related to the observations from the 3-springs configuration analysis. As we have previously mentioned, a larger value of the K_2 spring angle θ_0 in a 3-spring configuration does not result in a larger value of the figure of merit. This is consistent with the optimal geometries for the architected material implementation: for all optimal designs, we find $h/0.5L = 0.04 - 0.11$ and $h/t_2 = 3 - 4$; these values are not very high, and the ratio h/t_2 is very close to the minimum

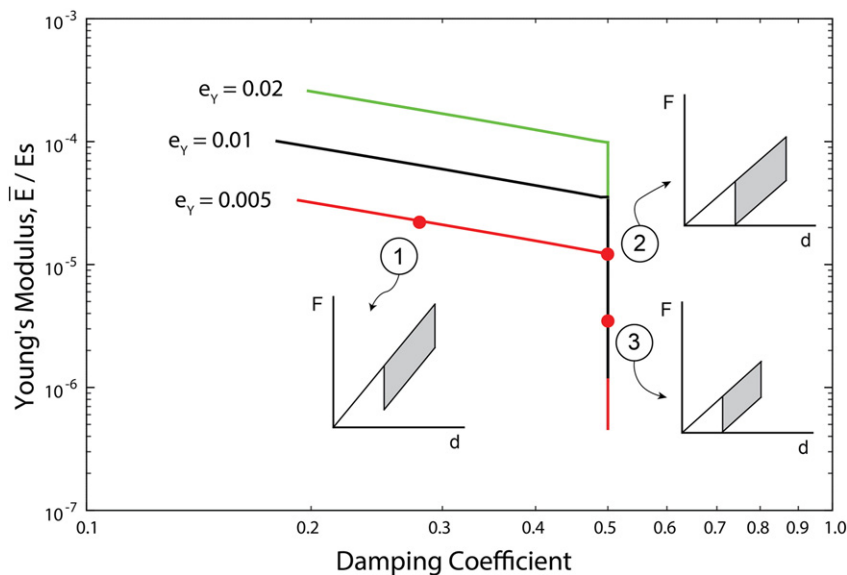


Fig. 8. Optimized stiffness/damping response for the architected material implementation of the 3-spring configuration. Each curve represents a different value of yield strain of the constituent material. Note that the figure of merit, Π , is constant along the diagonal section, until a value of $\psi = 0.5$ is reached. From that point forward, ψ remains constant and the stiffness drops, inducing a drop in the figure of merit. The insets qualitatively show force-displacement curves corresponding to three specific designs.

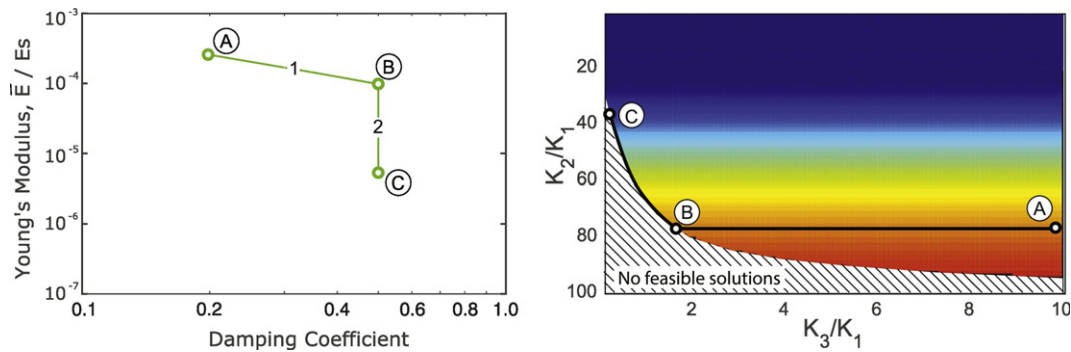


Fig. 9. Relation between the optimal performance of the architected material implementation of the 3-spring configuration (presented in Fig. 8) and its general mechanical model (presented in Fig. 4). Along the diagonal line (1) the designs maintain a constant value of K_2/K_1 while K_3/K_1 is reduced from A to B; in this region, the stiffness is decreased from A to B, while the loss factor is increased. At point B, the recoverability limit is reached, and the optimal designs must skirt the limit of recoverability from B to C, resulting in a progressive reduction in stiffness without any increase in loss factor.

value required to have vertically symmetric buckling. In other words, steep arches are not required for optimal performance.

4. Conclusions

In this paper, we present a detailed mechanical analysis of a three-spring mechanical model under quasi-static cyclic loads, and show that the presence of an internal degree of freedom in the system provides a substantial amount of energy dissipation upon cyclic loading, even when fabricated with linear elastic materials with only limited intrinsic damping. The analytical model is used to rigorously investigate the effect of each geometric and materials parameter on the mechanical performance, and identify optimal geometries for maximum energy dissipation. In particular, we observe that proper selection of the ratio of the negative spring stiffness (K_2) to the stiffness of the positive spring in series with it (K_1) is crucial to ensure optimal energy dissipation: in particular, energy dissipation monotonically increases with increasing the ratio K_2/K_1 , but an upper bound of K_2/K_1 is imposed by the recoverability constraint.

Compared to previously published snap-through-based designs for energy dissipation, which largely consisted of multiple identical bistable elements arranged in series [9,10,21,22], the proposed three-spring configuration presents multiple important advantages: (i) the addition of the spring K_3 allows for much stiffer designs; (ii) the addition of K_1 introduces an extra degree of freedom, which can be used to maximize the amount of energy dissipation or carefully tune the snap-through displacement; (iii) the combined addition of K_1 and K_3 offers the possibility to design lossy architected materials with recoverable behavior, even when K_2 is bistable (as discussed in this work); (iv) the combined presence of K_1 and K_3 ensures that hysteresis occurs even within a single unit cell, whereas traditional K_2 designs require a large number of unit cells for energy dissipation [9].

Subsequently, we present a particular implementation of the 3-spring model as the unit cell of a periodic architected material. The specific configuration is chosen so that it can be easily fabricated in a single base material by additive manufacturing techniques, e.g. brazing or 3D printing, and do not require any external pre-compression of the springs, or any pin joints, in order to achieve negative stiffness. All springs are implemented by arches, resulting in an architected material that is bending dominated under the applied loads considered in this study. This allows for substantial tunability of the range of motion, a critical condition for several structural applications. Conceptually similar stretching dominated configurations are currently under development and will be presented elsewhere.

The analytical model developed for the generic 3-spring mechanical model is applied to the particular implementation, and the predicted load-displacement curve obtained under cyclic loading is verified with

numerical models (Finite Elements Analyses) and validated with a cyclic compression experiment on a 3D printed prototype. The validated analytical model is then used for optimal design studies, where architected materials with optimal values of the figure of merit ψ , defined as the product of Young's modulus, E and loss coefficient, ψ . We show that the maximum achievable value of the figure of merit is proportional to the Young's modulus and to the yield strain of the constituent material. Another important remark is that for our specific architected material implementation, the limiting constraint is the yield strength of the K_2 arch; clearly, the thicker the arch, the more difficult it will be to achieve snap-through without yielding. Once the optimal dimensions of the K_2 arch are obtained, the figure of merit could be further increased by stacking multiple arches of identical dimensions on top of each other; as each arch would experience the same maximum stress (which in an optimized system would be equal to the yield strength of the material), the constraint would not be violated, whereas the figure of merit would increase proportionally to the number of arches. Clearly this assumes that the stiffness of the spring K_1 could be increased proportionally to K_2 as needed without violating manufacturing constraints, and that the recoverability constraint can still be met (i.e., $\psi < 0.5$). An alternative approach for further increasing the figure of merit is replacing the arch with a structural element with higher negative stiffness.

In conclusion, we demonstrate a flexible approach to architected material design that allows for tailorable combinations of high stiffness, low density and high energy dissipation by enhancing the host materials inherent damping. The proposed architected material can be designed to exhibit single or bi-stability and can be implemented with any constituent material at virtually any length scale. Several additive manufacturing approaches can be adopted for fabrication, depending on the constituent material and the unit cell size. The energy dissipation mechanism employed here does not require additional damping specific materials, nor does it require a large number of unit cells, and the proposed architected material can be fabricated from virtually any constituent material, potentially allowing use under high temperatures or aggressive environmental conditions. Future developments include a stretching dominated lattice material implementation, for improved performance.

Acknowledgments

Funding from Office of Naval Research (Program Manager: D. Shifler, Contract No. N000141110884) is gratefully acknowledged. AGI would like to thank the Obra Social "la Caixa" for partial financial support. AGI and RFA are also thankful to the Balsells Foundation for partial financial support. The Abaqus Finite Element Analysis software is licensed from Dassault Systemes SIMULIA, as part of a Strategic Academic Customer Program between UC Irvine and SIMULIA.

Appendix A. Stiffness and strength of the arch-shaped springs

Here we present the approach that is used to obtain close-form solutions for the stiffness of elements K_{11} and K_3 (the positive stiffness elements) in the cellular material implementation of the 3-spring model. As both springs are arches, which are primarily bending dominated, we invoke dimensional analysis supported by beam theory to conclude that the stiffness of each arch will be proportional to the Young's modulus of the constituent material, E_s , the width of the arch and the cube of the thickness/length ratio, i.e.:

$$\frac{K_1}{E_s \cdot W_1} = a \left(\frac{t_1}{l_1} \right)^3 \quad (\text{A.1})$$

$$\frac{K_3}{E_s \cdot W_3} = b \left(\frac{t_3}{R_3} \right)^3 \quad (\text{A.2})$$

where a and b are non-dimensional coefficients. The numerical values of the two coefficients a and b are obtained by fitting of Finite Elements analyses performed in ABAQUS. Both arches are modeled with 2D solid elements with linear elastic material, and subjected to an end displacement in the vertical direction equal to $0.2 \cdot l_1$ and $0.4 \cdot R_3$ for K_1 and K_3 , respectively. All analyses are quasi-static and non-linear. A number of simulations are performed with arches of different thickness, and the axial stiffness of the arch (force/displacement at the end of the loading cycle) is plotted against the arch thickness. A cubic fit provided the values of the parameters a and b , namely $a = 1.38$ and $b = 0.46$ (See Fig. A1). Notice that the cubic fit expressed in Eqs. (A.1)–(A.2) is in excellent agreement with the FE results.

The strength of both elements was also modeled by dimensional analysis using beam theory, with fitting coefficients obtained by Finite Elements simulations. The geometry of element K_1 can be simplified as a quarter of a circle, with the bottom end clamped and the top end allowed to freely rotate, as schematically depicted in Fig. A2. The maximum stress will clearly occur at the mid-section, on the inside of the arch. If we assume that the whole element is under an axial displacement Z , the applied force at the mid-section (quarter of the circle) will be $F = K_1 \cdot Z$. The maximum stress is a combination of the axial and bending stress, and can be expressed as:

$$\begin{aligned} \sigma_{\max}^{K_1} &= \frac{F}{A} + \frac{F \cdot R_1 \cdot t_1}{I \cdot 2} = \frac{K_1 \cdot Z}{W_1 \cdot t_1} + \frac{K_1 \cdot Z \cdot 0.25 l_1 \cdot t_1}{I \cdot 2} \\ &= 2.06E \frac{t_1}{l_1^2} Z + 1.38E \frac{t_1^2}{l_1^3} Z \end{aligned} \quad (\text{A.3})$$

The element K_3 can be simplified as a quarter of circle, with the bottom clamped and the top end with the rotation constrained; this results in the establishment of a moment M_0 , as plotted in Fig. A2. The maximum stress will occur at the top end, and can be expressed as:

$$\sigma_{\max} = \frac{M_0 \cdot t_3}{I \cdot 2} \quad (\text{A.4})$$

We find the moment M_0 using Castigliano's theorem, imposing $\delta_\theta = 0$ at the top end. Consequently we find:

$$\sigma_{\max}^{K_3} = \frac{3}{\pi} E \frac{t_3}{R_3^2} Z \quad (\text{A.5})$$

The stiffness and maximum stress experienced by the arch K_2 (the negative stiffness element) were reported in [28].

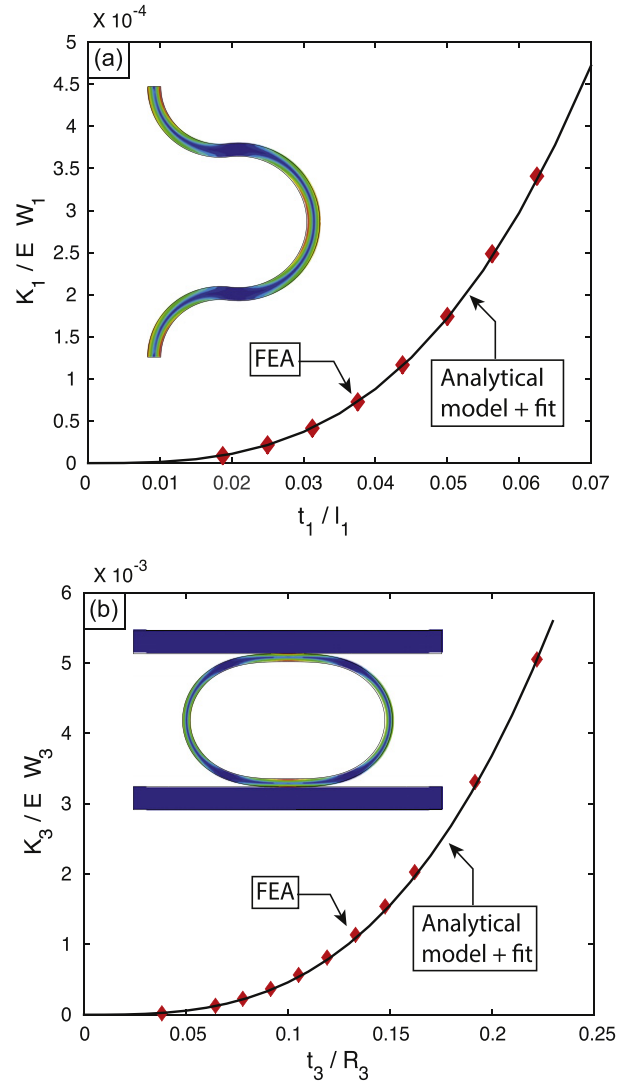


Fig. A1. (a) Plot of the stiffness of the K_1 element versus t_1/l_1 extracted by FEA (red diamonds), and fit to a cubic equation (solid black line). The inset shows the distribution of equivalent stresses in the compressed arch, at a given point in the simulation. (b) Plot of the stiffness of the K_3 element versus t_3/R_3 extracted by FEA (red diamonds), and fit to a cubic equation (solid black line). The inset shows the distribution of equivalent stresses in the compressed arch, at a given point in the simulation.

Appendix B. Mechanical characterization of the base material (ABS) printed by Fused Deposition Modeling

A prototype of the unit cell of the proposed periodic cellular material implementation is printed by Fused Deposition modeling in ABS using a Flashforge Creator Pro (see Section 2.4 for details). In order to correctly characterize our prototype and ensure that none of the elements yield under the design loading-unloading cycle, it is essential to measure the base material properties. Dog-bone tensile specimen in agreement with the ASTM D638–014 standard are printed with the same Flashforge Creator Pro used for all architected material fabrication. All arch elements are printed separately to ensure fiber orientation along the length of the arch; hence, dogbone test coupons are only printed with fibers aligned with the loading direction. The Young's modulus of printed ABS is extracted using the strain measured by a strain gage (Fig. B1), and is reported as $E = 1.74$ GPa. The yield strain of printed ABS is measured using the displacement reading of the universal testing

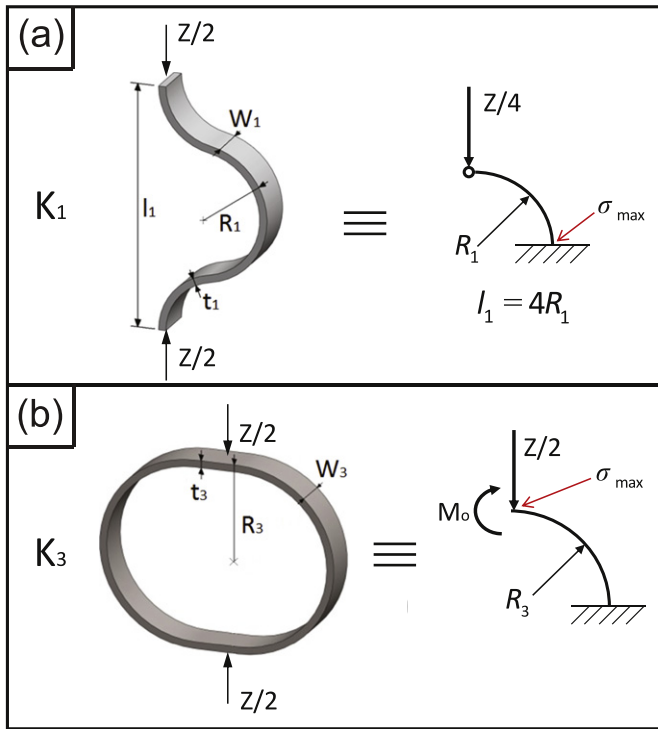


Fig. A2. Schematic of the arch implementation for K_1 and K_3 , with geometric variable definitions and mechanical model used in analytical stress calculations.

machine and the 0.2% residual strain rule (Fig. B1), and is reported as $\epsilon_y = 0.016$. To ensure that our material remains elastic throughout the complete loading-unloading cycle, we will impose that no element ever reach a strain higher than $\epsilon = 0.01$.

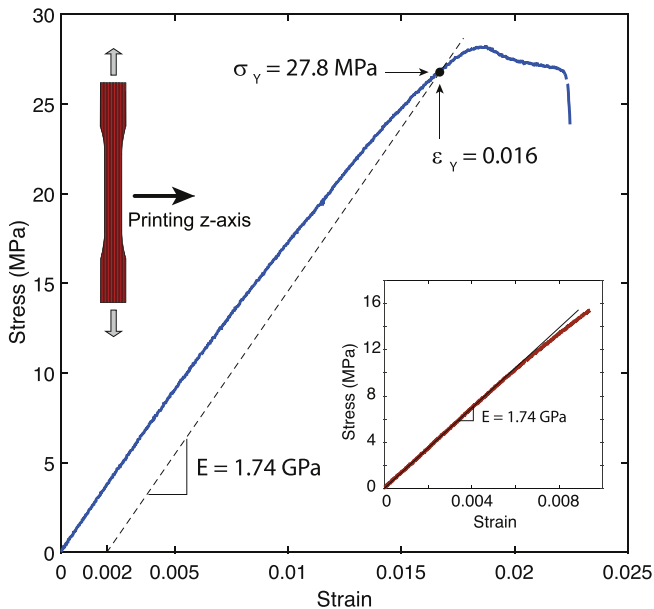


Fig. B1. Results of the tensile test ABS printed by Fused Deposition Modeling. The direction of printing is shown. In the experiment in red, the strain measurements are obtained using a strain gage, and from these results we extract the Young's Modulus. In the experiment in blue, the strain has been calculated from the displacement readings of the universal testing machine, and we use these results to calculate yield strength and yield strain using the 0.2% residual strain rule.

Appendix C. Performance and geometric parameters of optimal lattice structures

As explained in Section 3.1, the optimization scheme proceeds as follows: the effective Young's modulus of the lattice, \bar{E} , is swept in the chosen range. For every value of \bar{E} , the optimizer identifies the best combination of 5 independent variables (K_1 (N/mm), K_3 (N/mm), W_2 (mm), t_2 (mm) and h (mm)) that maximizes the loss coefficient, ψ . The Young's modulus of the parent material is set at $E_s = 2$ GPa, and the optimization studies are repeated for three different values of the yield strain of the parent material ($\epsilon_y = 0.005, 0.01, \text{ and } 0.02$). The length of the bi-stable element, L is kept constant at 100 mm.

The optimization results are reported in Table A1 (some intermediate values were omitted for conciseness). Notice that a decrease in \bar{E} induces a simultaneous decrease in K_1, K_3, h and t_2 . Also notice that for all optimal designs, $h/0.5L = 0.04 - 0.11$ and $h/t_2 = 3 - 4$.

Once the optimal values of the primary variables are determined, Eqs. (A.1) and (A.3) are used to select suitable values of t_1, W_1, l_1 and Eqs. (A.2) and (A.5) are used to select suitable values of t_3, W_3, R_3 .

Table C1

Optimal geometries leading to the results summarized in Fig. 8. Please refer to Fig. 5a for variables definition (several intermediate rows were omitted for conciseness).

$\bar{E} \times 10^{-5}$	ψ	K_3 (N/mm)	K_1 (N/mm)	W_2 (mm)	t_2 (mm)	h (mm)
$\epsilon_y = 0.005$						
3.25	0.20	1.24	0.91	30.00	0.80	2.64
1.50	0.43	0.36	0.91	30.00	0.80	2.64
1.25	0.50	0.25	0.88	29.71	0.82	2.55
1.00	0.50	0.19	0.73	24.23	0.83	2.50
0.50	0.50	0.11	0.31	29.99	0.56	2.05
0.40	0.50	0.08	0.27	29.83	0.55	1.77
0.30	0.50	0.07	0.19	29.44	0.48	1.73
0.20	0.50	0.04	0.14	29.47	0.44	1.41
0.10	0.50	0.02	0.08	17.27	0.45	1.28
$\epsilon_y = 0.01$						
10.00	0.18	3.90	2.57	30.00	1.13	3.74
5.00	0.37	1.40	2.57	30.00	1.13	3.74
3.50	0.50	0.70	2.51	30.00	1.16	3.56
3.00	0.50	0.60	2.14	26.47	1.14	3.53
2.50	0.50	0.34	2.33	29.73	1.20	3.19
2.00	0.50	0.45	1.23	29.99	0.89	3.32
1.50	0.50	0.31	1.02	29.97	0.85	2.76
0.50	0.50	0.12	0.29	25.45	0.57	2.53
0.25	0.50	0.04	0.20	29.55	0.51	1.46
$\epsilon_y = 0.02$						
25.00	0.21	9.38	7.27	30.00	1.60	5.28
12.50	0.41	3.13	7.27	30.00	1.60	5.28
10.00	0.50	2.05	6.94	30.00	1.61	5.13
7.50	0.50	1.40	5.69	23.28	1.68	4.93
3.50	0.50	0.80	2.08	25.46	1.11	4.49
2.50	0.50	0.55	1.56	21.87	1.07	3.91
1.50	0.50	0.22	1.35	25.38	1.05	2.81
1.00	0.50	0.17	0.82	21.74	0.91	2.56
0.50	0.50	0.10	0.36	29.65	0.61	1.87

References

- [1] S.D. Papka, S. Kyriakides, In-plane compressive response and crushing of honeycomb, *J. Mech. Phys. Solids* 42 (1994) 1499.
- [2] S.R. Reid, Plastic deformation mechanisms in axially compressed metal tubes used as impact energy absorbers, *Int. J. Mech. Sci.* 35 (1993) 1035.
- [3] B. Samali, K.C.S. Kwok, Use of viscoelastic dampers in reducing wind- and earthquake-induced motion of building structures, *Eng. Struct.* 17 (1995) 639.
- [4] R.S. Lakes, *Viscoelastic Materials*, Cambridge University Press, 2009.
- [5] L. Salari-Sharif, T.A. Schaedler, L. Valdevit, Energy dissipation mechanisms in hollow metallic microlattices, *J. Mater. Res.* 29 (2014) 1755.
- [6] L.R. Meza, S. Das, J.R. Greer, Strong, lightweight, and recoverable three-dimensional ceramic nanolattices, *Science* 345 (2014) 1322.

- [7] P. Liu, Q. Tan, L. Wu, G. He, Compressive and pseudo-elastic hysteresis behavior of entangled titanium wire materials, *Mater. Sci. Eng. A* 527 (2010) 3301.
- [8] B. Gadot, O.R. Martinez, Roscoat du SR, D. Bouvard, D. Rodney, L. Orgéas, Entangled single-wire NiTi material: a porous metal with tunable superelastic and shape memory properties, *Acta Mater.* 96 (2015) 311.
- [9] D. Restrepo, N.D. Mankame, P.D. Zavattieri, Phase transforming cellular materials, *Extrem. Mech. Lett.* 4 (2015) 52.
- [10] D.M. Correa, C.C. Seepersad, M.R. Haberman, Mechanical design of negative stiffness honeycomb materials, *Integ. Mater. Manuf. Innov.* 4 (2015).
- [11] R.S. Lakes, Extreme damping in compliant composites with a negative-stiffness phase, *Philos. Mag. Lett.* 81 (2001) 95.
- [12] P.M. Alabuzhev, E.I. Rivin, *Vibration Protection and Measuring Systems With Quasi-zero Stiffness*, CRC Press, 1989.
- [13] X. Liu, X. Huang, H. Hua, On the characteristics of a quasi-zero stiffness isolator using Euler buckled beam as negative stiffness corrector, *J. Sound Vib.* 332 (2013) 3359.
- [14] D.F. Ledezma-Ramirez, N.S. Ferguson, M.J. Brennan, An experimental nonlinear low dynamic stiffness device for shock isolation, *J. Sound Vib.* 347 (2015) 1.
- [15] N. Hu, R. Burgueño, Buckling-induced smart applications: recent advances and trends, *Smart Mater. Struct.* 24 (2015), 063001.
- [16] A. Carrella, M.J. Brennan, T.P. Waters, Static analysis of a passive vibration isolator with quasi-zero-stiffness characteristic, *J. Sound Vib.* 301 (2007) 678.
- [17] C.M. Lee, V.N. Goverdovskiy, A.I. Temnikov, Design of springs with "negative" stiffness to improve vehicle driver vibration isolation, *J. Sound Vib.* 302 (2007) 865.
- [18] T.D. Le, K.K. Ahn, A vibration isolation system in low frequency excitation region using negative stiffness structure for vehicle seat, *J. Sound Vib.* 330 (2011) 6311.
- [19] A.A. Sarlis, D.T.R. Pasala, M.C. Constantinou, A.M. Reinhorn, S. Nagarajaiah, D.P. Taylor, Negative stiffness device for seismic protection of structures, *J. Struct. Eng.* 139 (2013) 1124.
- [20] N. Zhou, K. Liu, A tunable high-static-low-dynamic stiffness vibration isolator, *J. Sound Vib.* 329 (2010) 1254.
- [21] A. Rafsanjani, A. Akbarzadeh, D. Pasini, Snapping mechanical metamaterials under tension, *Adv. Mater.* 27 (2015) 5931.
- [22] S. Shan, S.H. Kang, J.R. Raney, P. Wang, L. Fang, F. Candido, et al., Multistable architected materials for trapping elastic strain energy, *Adv. Mater.* 27 (2015) 4296.
- [23] L. Dong, R.S. Lakes, Advanced damper with negative structural stiffness elements, *Smart Mater. Struct.* 21 (2012), 075026.
- [24] I. Antoniadis, D. Chronopoulos, V. Spitas, D. Koulocheris, Hyper-damping properties of a stiff and stable linear oscillator with a negative stiffness element, *J. Sound Vib.* 346 (2015) 37.
- [25] I.A. Antoniadis, S.A. Kanarachos, K. Gryllias, I.E. Sapountzakis, K. Damping, A stiffness based vibration absorption concept, *J. Vib. Control.* (2016) <http://dx.doi.org/10.1177/1077546316646514>.
- [26] D. Chronopoulos, I. Antoniadis, M. Collet, M. Ichchou, Enhancement of wave damping within metamaterials having embedded negative stiffness inclusions, *Wave Motion* 58 (2015) 165.
- [27] T.A.M. Hewage, K.L. Alderson, A. Alderson, F. Scarpa, Double-negative mechanical metamaterials displaying simultaneous negative stiffness and negative Poisson's ratio properties, *Adv. Mater.* 28 (2016) 10323.
- [28] J. Qiu, J.H. Lang, A.H. Slocum, A curved-beam Bistable mechanism, *J. Microelectromech. Syst.* 13 (2004) 137.